# In situ pH measurements of individual levitated microdroplets using aerosol optical tweezers

Boyer, Hallie.C.<sup>1,†</sup>; Gorkowski, Kyle<sup>2</sup>; Sullivan, Ryan C.<sup>1,\*</sup>

<sup>1</sup>Center for Atmospheric Particle Studies, Carnegie Mellon University, Pittsburgh, PA, USA.

<sup>2</sup>Department of Atmospheric and Oceanic Sciences, McGill University, Montreal, Quebec, Canada.

†Present address: Department of Mechanical Engineering, University of North Dakota, Grand Forks, ND, USA. \*Corresponding Author: R.C. Sullivan (<u>rsullivan@cmu.edu</u>)

# Author contact information:

Hallie C. Boyer

Email: Hallie.chelmo@und.edu

Phone: (701) 777-6515

Orcid: https://orcid.org/0000-0002-7193-1465

Kyle Gorkowski

Email: kyle.gorkowski@mcgill.ca

Orcid: https://orcid.org/0000-0002-3750-1189

Ryan C. Sullivan

Email: rsullivan@cmu.edu Phone: (412) 268-8462

Orcid: 0000-0003-0701-7158

### Abstract

The pH of microscale reaction environments controls numerous physicochemical processes, requiring a real-time pH micro-probe. We present highly accurate real-time pH measurements of microdroplets using aerosol optical tweezers (AOT) and analysis of the Whispering Gallery Modes (WGMs) contained in the cavity-enhanced Raman spectra. Uncertainties ranging from ±0.03 to 0.06 in pH for picoliter droplets are obtained through averaging Raman frames acquired at 0.5 Hz over 3.3 minutes. The high accuracy in pH determination is achieved by combining two independent measurements uniquely provided by the AOT approach: the anion concentration ratio from the spontaneous Raman spectra, and the total solute concentration from the refractive index retrieved from WGM analysis of the stimulated cavity-enhanced Raman spectra. pH can be determined over a range of -0.36 to 0.76 using the aqueous sodium bisulfate system. This technique enables direct measurements of pH-dependent chemical and physical changes experienced by individual microparticles, and exploration of the role of pH in the chemical behavior of confined microenvironments.

The activity of the hydrogen ion in solution ( $a_{H^+}$ ) influences chemical thermodynamics and microdroplet transformations. It is measured on the pH scale (=-log<sub>10</sub>[a<sub>H+</sub>]) and plays critical roles in compound solubilities, phase separations and phase transitions,<sup>1,2,3</sup> emulsion stability,<sup>4</sup> and reaction rates in the aqueous phase<sup>5–10</sup> and on surfaces.<sup>11</sup> The inability to directly determine the pH of individual microdroplets creates a major measurement blind spot that inhibits our understanding of chemical microenvironments, and the role of aerosol particles in driving heterogeneous chemistry in the atmosphere.

In this work, we present an advanced in situ technique for highly accurate real-time pH measurements of levitated picoliter microdroplets in an aerosol optical tweezers, using the aqueous sulfate/bisulfate system. Coddens et al.<sup>12</sup> also used an aerosol optical tweezers to stably levitate and trap aqueous aerosol particles; they successfully demonstrate titration of trapped particles by coalescence of droplets containing strong acids. They solely use spontaneous Raman modes for sulfate and carbonate anions calibrated with bulk measurements to measure concentrations of the individual anion without the use of WGMs to determine total solute concentration. Instead, they assume that droplet concentration is invariant in the AOT chamber unless introduced to another liquid through coalescence. To account for non-ideal thermodynamics, they use these measured concentrations coupled with long-range (Debye-Huckel theory) and short-range (specific ion interaction theory) electrostatic interactions to solve for activity coefficients for H<sup>+</sup>, and therefore obtain a<sub>H+</sub>. Our novel approach uses two independently measured quantities measured from the Raman spectrum obtained in AOT experiments: calibrated peak area ratios of the acid and conjugate base vibrational modes, and the refractive index retrieved by analysis of the Whispering Gallery Modes (WGMs) from the stimulated cavity-enhanced Raman spectrum. The solute concentration determined from the highly accurate refractive index measurements provides valuable information for determining the proton activity and accounting for non-ideal interactions in these high ionic strength microdroplets. This online method measures microdroplet pH as the particle is stably levitated, while prior pH measurements of aerosol droplets, other than the recent work by Coddens et al.,<sup>12</sup> are limited to pre-collected particles that require particle-surface contact. Our real-time measurements enable exploring dynamic changes such as the effects of heterogeneous chemistry on pH and the resulting change in microparticle structure.

In microscopically confined environments, the effects of solution pH on solute charge states and solubilities result in unique, but poorly understood, chemical and physical phenomena, otherwise well known in bulk solutions. Confined environments refer to the picoliter volumes of the systems in question, such as in particulate suspensions, colloids, biological cells, and other complex fluids. Aerosol droplets, for example, exhibit pH-dependent physical and chemical processes that differ from their bulk counterparts because of their confined nature and high surface area-to-volume ratio, including phase separation, <sup>1,2</sup> prolonged metastable states such as supercooled and supersaturated with respect to solute, <sup>14</sup> accelerated chemical reaction rates, <sup>10,15–17</sup> and gas-surface chemical reactive uptake. <sup>11</sup> Particle acidity plays a crucial role in all these processes, yet the interplay of these pH effects has not been directly observed and quantified.

Aqueous droplets can act as microreactors in which chemical reactions occur at rates up to five orders of magnitude greater than in the bulk, 15,18 where the rate constant scales inversely with droplet radius. 19 These microreactors can even facilitate chemical pathways that do not occur at all in the bulk, such as the production of sugar phosphates relevant to prebiotic broth theory. 20 Recently, Jacobs et al. 6 studied chemical reactions that only occur in droplets and they linked the pH accelerated reaction rates to the interfacial composition. The key implication is that the interfacial effects enable a different reaction mechanism that lowers the reaction energy barrier. 5,9

Although experimental studies are progressing towards a fundamental understanding of microdroplet chemistry, pH effects have not been directly observed and quantified as we lack *in situ* methods for direct pH measurements of droplets in real-time.<sup>21</sup>

Aside from microdroplets, localized pH is important for protein denaturation and enzyme structure, for pharmaceutical synthesis, crystallization, and delivery,<sup>22</sup> and in understanding fatal neurological diseases in mammals caused by prion misfolding.<sup>23</sup> pH governs micelle formation in soaps and foams, confining the influence of pH to nanoscales and distributing pH from the aqueous core to the lipid layer.<sup>24</sup> Changes in pH from a droplet's center to its surface have been explored experimentally revealing a gradient of 2-3 pH units.<sup>7,25</sup> Also, the pKa value of organic acid surfactants varies between the surface and the bulk.<sup>26</sup> The purported internal variation of droplet acidity and degree of dissociation suggests the importance of chemical locality, such as in the surface region, but the concept of pH in environments where the number of water molecules is fewer than 10<sup>7</sup> molecules is poorly defined.<sup>24</sup> Experimental techniques to interrogate particles *in situ*, towards characterizing the acidity of trapped isolated particles, are needed to directly determine pH and its critical role in this myriad of chemical phenomena.

An improved understanding and quantification of the pH of microdroplets suspended in the ambient environment, collectively known as atmospheric aerosol, is required because of the important role that particulate matter plays in climate and ecosystem health effects. They act as seeds for cloud droplets and nucleation points for ice crystallization of cloud particles. These two aspects change cloud microphysics and radiative properties, and thus profoundly affect the global energy balance. Acidic droplets exhibit harmful effects on marine and terrestrial ecosystems and human health, as well as providing a vector for nutrient delivery to remote ocean regions due to the dissolution of iron (pH<4).<sup>27</sup> Further, pH influences the solubility of ions and organic and

inorganic acids, as well as heterogeneous reactions with trace gases, e.g. aqueous oxidation of gaseous SO<sub>2</sub> to H<sub>2</sub>SO<sub>4</sub>.<sup>28</sup> pH also influences solution reaction kinetics of oxidation, hydrolysis, and oligomerization. Sulfate production is highly pH dependent, yet the precise ranges of atmospheric aerosol pH that determine the particle-phase chemical production mechanisms of H<sub>2</sub>SO<sub>4</sub> are currently under debate with important consequences on our understanding of atmospheric chemistry and the controlling chemical factors for air quality.<sup>29</sup> Intense sulfate aerosol production in China contributes to severe haze events and ambient aerosol pH must be known to determine the production mechanisms.<sup>30,31</sup> Different atmospheric aerosol pH ranges are reported - from 5.4 to  $6.2^{30}$  and 3.0 to  $4.9^{31}$  - possibly due to thermodynamic model estimates that neglect organic component contributions and the inaccessibility of direct measurements. Acidic conditions also limit the type of photochemical processes and products feasible in aerosol particles and their rates of formation.<sup>32</sup> Despite the prevalence of acidic aerosol in the atmosphere, aerosol droplet pH is only inferred from indirect estimates based on other measurements, dilution, and statistical averaging over particle populations.<sup>33,34</sup> Understanding how acidity effects chemical reactions and phase separation in aerosol particles, if well characterized, would reduce uncertainties in model estimates of atmospheric aerosols and their impacts on climate change, atmospheric chemistry, and health effects.

pH measurements have become increasingly localized using microspectroscopic techniques. Prior laser-induced droplet pH measurements approaches include fluorescence,<sup>35</sup> Raman microscopy,<sup>36,37</sup> and surface-enhanced Raman spectroscopy (SERS).<sup>7</sup> Sayer et al.<sup>35</sup> used fluorescence synchronized with a train of generated aerosol droplets doped with fluorescent dye. Rindelaub et al.<sup>37</sup> developed a method for direct measurements of droplet pH using Raman microspectroscopy, where each individual acid and conjugate base concentration was calibrated

against the integrated peak area. Proton concentration was then determined from known equilibrium dissociation constants. Craig et al.<sup>36</sup> successfully applied this technique to a breath of inorganic and organic acidic and alkaline pH probes, covering nearly the entire pH range. The aerosol particles were collected onto substrates prior to offline Raman microscopy. Wei et al.<sup>7</sup> also used offline techniques to study microdroplets on a substrate with SERS to enhance the otherwise weak Raman signal. Water droplets were doped with noble metal nanoparticles to maximize the SERS-active surface area, as well as to create a suspension that enabled 3D confocal microscopy for spatial resolution. They found that pH gradually decreases by close to 3 units from the droplet's alkaline center to the surface. These previous advances have proven the efficacy and versatility of spectroscopic techniques for offline microdroplet pH measurements. To further study the evolving processes that changes in pH induce in suspended microdroplets, an *in situ* contact-free method for measuring microdroplet pH in real-time is required.

The challenges associated with direct measurements of particle pH and simultaneous observation of pH dependent processes are that physical contact with the particle changes its surface energy, and thus its morphology, and that their small volumes prohibit conventional laboratory pH probes. Indirect and offline methods are often used to estimate suspended microdroplet pH instead. These have yielded discrepancies among thermodynamic model predictions, and laboratory and ambient measurements of atmospheric aerosols.<sup>33</sup> Here we demonstrate the use of aerosol optical tweezers and the resulting cavity-enhanced Raman spectrum to obtain high accuracy real-time pH measurements of stably levitated individual microdroplets.

# **Experimental Section**

Aerosol optical tweezers methods and materials.

Aerosol optical tweezers produce a contact-free, stable optical trap that probes and isolates growth processes, phase transitions, microstructure, and chemical reactions<sup>5,6,8,38,39</sup> experienced by trapped individual microdroplets. Optical tweezers use a tightly focused laser beam to stably trap a single particle and simultaneously stimulate and retrieve the Raman spectrum from the particle.<sup>4,40–45</sup> When a dielectric particle encounters the strong electric field near the laser beam waist, the particle becomes trapped through a balance of scattering and gradient forces. The Raman signal is then produced from inelastic scattering of the trapping laser by the droplet. In spherical particles, surface resonant standing waves akin to Whispering Gallery Modes (WGMs) produce greatly enhanced stimulated signal at discrete wavelengths over the spontaneous broadband Raman modes. Using Mie scattering theory, analysis of WGM wavelength positions enable highly accurate retrievals of refractive index within 0.06% and radius within 0.05% in real-time.<sup>4,44,45</sup> The unique real-time analytical capabilities of aerosol optical tweezers systems have been detailed in numerous prior studies.<sup>4,40–45</sup>

For trapped acidic microdroplets, the Raman mode for the acid and conjugate base reflects the equilibrium concentration ratio, while total solute concentrations are derived from refractive indices retrieved from WGM analysis. This combined analysis is required to constrain the thermodynamic model used to derive pH from the acid:base concentration ratio, with the total solute concentration. Raman peak area ratios directly probe the chemical environment, explicitly providing acid:base concentration ratios for pH measurements. The advanced *in situ* technique developed here will inform pH-dependent physical and chemical processes in microdroplets.

We use a custom aerosol optical tweezers system (AOT) developed at Carnegie Mellon University and described by Gorkowski et al.<sup>45</sup> Briefly, aerosol generated from a nebulizer (PARI TREK S) and a controlled mixture of dry and humid air flow into the top of the chamber. A 532

nm trapping laser is directed through an expansion lens to fill the aperture of a 100x (NA 1.25) microscope objective at the base of the chamber, forming a tightly focused single gradient force optical trap. The nebulized aerosol is flowed into the chamber and down over the optical trap to produce a tweezed aerosol droplet. Laser power is typically around 50-80 mW and trapped aqueous particles are 3-5 µm in radius. Raman signal induced by the trapping laser is collected by the same objective, filtered to remove the trapping beam, and directed into the spectrometer (Princeton Acton spectrograph with PIXIS CCD detector), which records spectra at 0.5 Hz using a diffraction grating of 1200 g/mm. The spectral resolution of the system is 1.2 cm<sup>-1</sup>.

Previously, Gorkowski et al.  $^{44,45}$  and Preston et al.  $^{46,47}$  developed analysis of WGMs stimulated over the O–H and C–H stretch modes in homogeneous and biphasic core–shell particles. We used this analysis to fit particle radius and refractive index (650 nm, corresponding to the center of the water O–H Raman mode) through a range of relative humidity from 50-95%. In this work, WGMs sweep through the spectral range of the  $SO_4^{2-}$  and  $HSO_4^{-}$  spontaneous stretch modes and the prior WGM analysis algorithm of Gorkowski et al.  $^{45}$  retrieves radius and refractive index, as well as dispersion (dn/d $\lambda$ ). Droplet solute concentrations are then determined from empirical correlations with refractive index.  $^{48}$  The high accuracy of the refractive index measurements (0.06%) $^{44}$  enables determination of changes in solute concentration on the order of  $\pm 0.04$  M.

Calibration of the measured Raman mode peak area is presented in the Supporting Information (SI) and was performed using bulk Raman measurements of NaHSO<sub>4</sub> and Na<sub>2</sub>SO<sub>4</sub> solutions at two total solute concentrations (0.55 M and 3.5 M in Fig. S1a and S1c). The ratio of the peak areas for SO<sub>4</sub><sup>2-</sup>/HSO<sub>4</sub><sup>-</sup> correlates linearly with the concentration ratio of the two anions (Fig. S2). This linear relationship is applied to the peak area ratios in trapped droplets to convert to the concentration ratio.

The web-based Extended Aerosol Inorganics Model I (E-AIM)<sup>49–51</sup> was used to determine the proton activity ( $a_{H+}$ ) from the measured ion concentrations. Inputs to the E-AIM thermodynamic model are temperature, relative humidity, and the total concentration of aerosol chemical components. Gaseous species are possible inputs for E-AIM, but since our solutes are non-volatile gas-particle partitioning was not included.

### **Results and Discussion**

# **Direct pH Measurements of Levitated Microdroplets.**

We varied the relative humidity (RH) of the gas phase surrounding the tweezed droplet to vary the water content, and thus pH, without externally modifying the sodium bisulfate solute composition of the droplet. Direct pH measurements of high accuracy were achieved by combining the following approaches: (1) obtain the total solute concentration from the refractive index determined by WGM analysis; (2) calculate the integrated peak area ratio for the conjugate base and acid Raman modes,  $v(SO_4^{2-})/v(HSO_4^{2-})$ ; (3) convert the peak area ratio to the concentration ratio  $[SO_4^{2-}]/[HSO_4^{2-}]$ . Therefore, the pH measurements use both the relative concentration obtained from the peak area ratio in the spontaneous Raman modes and the total solute concentrations from analysis of the stimulated WGMs to directly measure the individual ion concentrations. (4) The solute concentration is then used to find the proton activity using the E-AIM aerosol thermodynamics model.<sup>49–51</sup> Finally, the expression pH =  $-\log(a_{H+})$  is used to determine particle pH, where  $a_{H+}$  is the molality-based proton activity – as defined by UNIFAC – converted from mole fraction-based activity coefficients output by E-AIM.

The inorganic  $SO_4^{2-}/HSO_4^{-}$  system is a suitable pH probe because it is non-volatile and has discernable Raman modes for the acid and conjugate base with center peaks at  $v(HSO_4^{-}) = 1050$  cm<sup>-1</sup> and  $v(SO_4^{2-}) = 980$  cm<sup>-1</sup>. A representative Raman spectrum for NaHSO<sub>4</sub> is shown in Figure

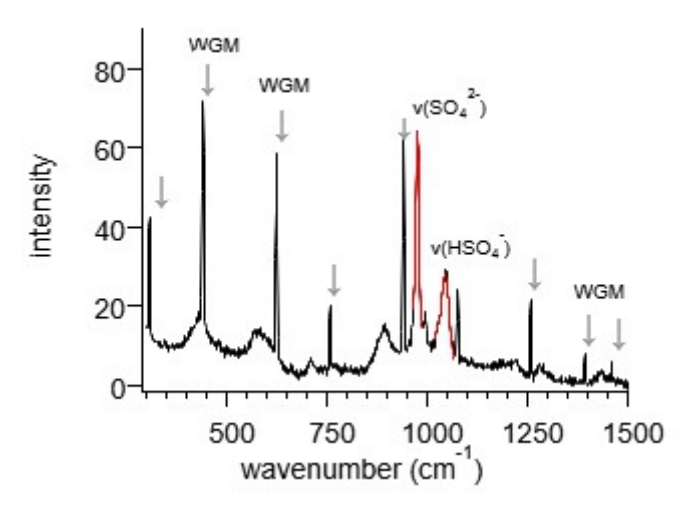


**Figure 1**: Representative cavity-enhanced Raman spectra from a tweezed aqueous droplet of 3.98 μm radius containing NaHSO<sub>4</sub>(aq). The spontaneous Raman vibrational stretch modes for HSO<sub>4</sub><sup>-</sup> and SO<sub>4</sub><sup>2</sup>- as well as the stimulated Whispering Gallery Modes (WGMs) resonant with the droplet are indicated. Spectra are the average of 100 spectral frames where the WGMs are stationary because of unchanging droplet size. Red traces are Gaussian fits indicating the integration range used to determine the Raman peak areas.

1. The spontaneous Raman modes for each ion and the stimulated WGMs are apparent. The WGMs change positions sensitively in response to particle size and refractive index (0.66 nm and 9.5\*10<sup>-5</sup> per unit wavenumber (cm<sup>-1</sup>) shift for droplet diameter and refractive index, respectively, within the typical size ranges and compositions). <sup>44</sup> Limits of integration do not to include the shoulder at 995 cm<sup>-1</sup> present in this representative spectrum. Although the shoulder was not present in all experiments, the limits of integration were kept constant for all bulk and AOT measurements for consistency. Previous spectroscopy work suggests the shoulder is possibly due to associated sodium sulfate salts, <sup>52,53</sup> but we only see the shoulder in the AOT, and not the bulk spectra at the same concentrations. It is unlikely that there are solid or undissolved salts in the droplet, especially given the lack of nucleation sites in the suspended droplet. Even if the shoulder arises because of Na<sub>2</sub>SO<sub>4</sub> associating in the particle, the accuracy of the sulfate and bisulfate Raman measurements is unaffected.

A time series for the Raman signal of a tweezed NaHSO<sub>4</sub>(aq) microdroplet is shown in Figure 2, featuring the positions and intensities of the acid and conjugate base modes, as well as the shifting WGMs in response to the changes in humidity and thus droplet radius and refractive index. In this way, Figure 2 shows how the pH of a single droplet can be probed using the relative intensities of the acid and base modes and stimulated WGMs provided in these time series as the surrounding relative humidity is varied. The WGMs are only present in the aerosol optical tweezers experiments and not in bulk or microspectroscopic Raman measurements on substrates. Aqueous droplets composed of inorganic solutes typically experience only mK increases in their temperature due to the very small imaginary refractive index of these components at the 532 nm trapping laser wavelength.<sup>54,55</sup> No evidence for droplet heating was observed, which would manifest as a sudden decrease in droplet size with a corresponding increase in refractive index due to water loss. As is evident from the experimental time series shown in Figure 2, the tweezed droplets are very stable, with relatively small changes in size that are induced by changing the relative humidity surrounding the droplet.

Figure 2 also illustrates a source of uncertainty in these measurements: when WGMs are present, they sometimes traverse the narrow spectral regions of the spontaneous anion Raman modes, yet only the spontaneous signal informs the concentration ratio. WGMs thus introduce noise to the concentration ratios, and we have not attempted to separate the resonant signal from the diffuse signal because when their mode wavelengths are closely overlapping, they are difficult to distinguish. This WGM effect is largely reduced by spectral averaging > 100 frames acquired at 0.5 Hz. In the broader vibrational modes such as the O–H and C–H stretches, WGMs are isolated using non-local means denoising algorithms and wavelet transforms. <sup>45</sup> Figure 2 shows an example of the spontaneous anion modes becoming very bright when the WGMs pass through, resulting in

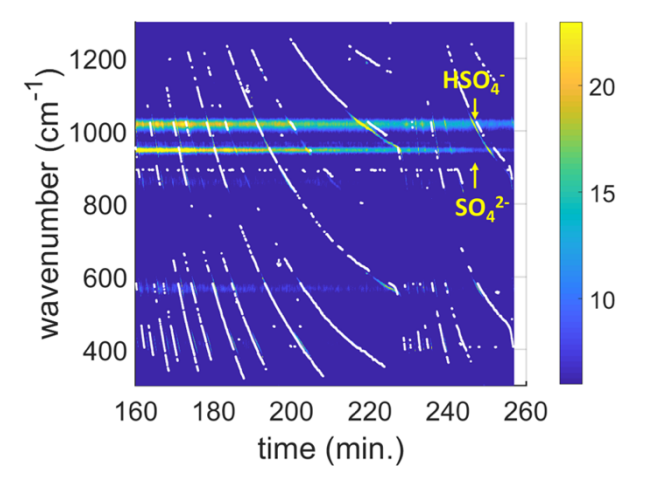


**Figure 2**: Raman shift (wavenumber, cm<sup>-1</sup>) timeseries for an NaHSO<sub>4</sub>(aq) droplet in the spectral range of the bisulfate anion ( $\nu$ (HSO<sub>4</sub><sup>-</sup>) = 1050 cm<sup>-1</sup>) and its conjugate base ( $\nu$ (SO<sub>4</sub><sup>2-</sup>) = 980 cm<sup>-1</sup>). The droplet has an initial size of 3.05 μm in radius, then evaporated down to 2.90 μm. The concentration of the NaHSO<sub>4</sub> solution from which the aerosol was nebulized was 8.0 M, therefore the acid peak is visibly stronger in intensity than the base peak. A 3.0 M solution droplet is shown in Figure S1 in the Supporting Information. WGMs identified by the analysis algorithm are indicated by the white streaks/dots as the particle undergoes changes in size through water partitioning with ambient humid air. Blue shifting of the WGM positions occurs as the droplet shrinks. The WGMs and relative strength of the acid and conjugate base Raman modes are used together to directly measure each microdroplet's pH.

an uncertainty in our concentration ratios of  $\pm 0.09$  with respect to bulk measurements when averaged over 100 frames.

Figure 3 shows the timeseries of the droplet radii and refractive indices retrieved from WGM analysis, as well as the resulting particle pH measurements for representative droplets. These experiments demonstrate that this pH measurement can directly track changes in the composition of the levitated droplet as it re-equilibrates with its changing environment. As droplet refractive index decreases towards the value of pure water (1.333), pH increases towards the ideal pK<sub>a</sub> value (2.0) for the HSO<sub>4</sub> anion. The droplet concentration dilutes when the particle freely uptakes water vapor. Droplet solute concentration increases as the particle loses water to a low RH chamber environment, but the trapped particle quickly decreases in size as well, and therefore at a certain

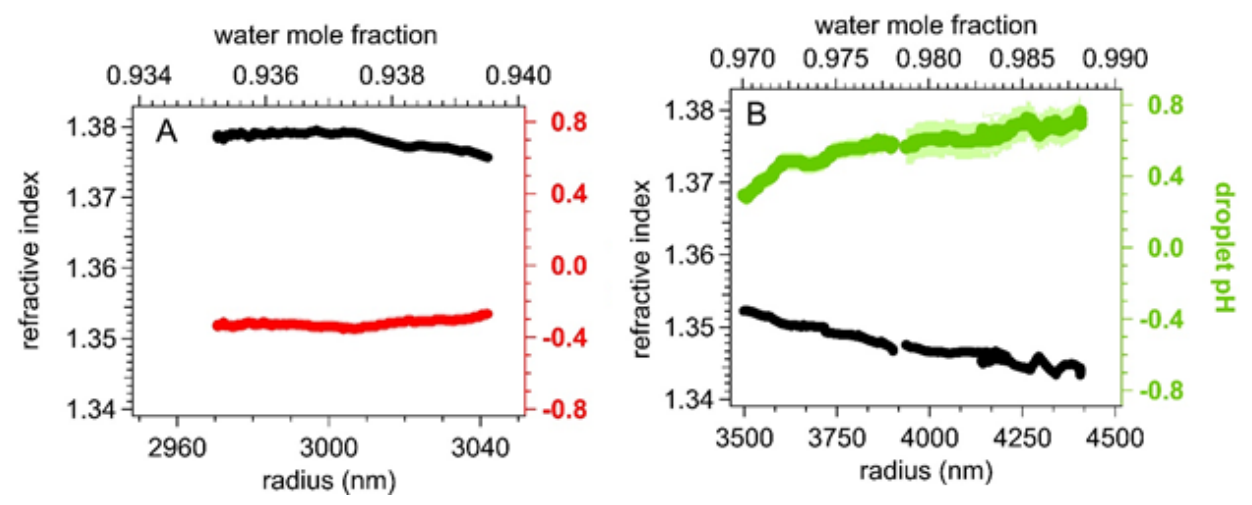


**Figure 3:** Refractive index (left y-axis, black) versus radius (bottom x-axis) and water mole fraction (top x-axis) from WGM analysis, and particle pH (right y-axis) versus radius (bottom x-axis) for two droplets (A: red, B: green) composed of aqueous NaHSO<sub>4</sub> that span the full range of concentrations and pH studied using the aerosol optical tweezers. The average molarity of each droplet is (A) 4.3 M and (B) 1.0 M. As radius increases, refractive index decreases due to water uptake and thus solute dilution. pH also increases as NaHSO<sub>4</sub> concentration dilutes. Moving averages were utilized with a sliding window length of 3.33 minutes, or 100 frames at 0.5 Hz. See Table S1 for details on the analysis and averaging of the Raman spectral frames, the total solute concentration ranges corresponding to the refractive indices, the concentration ratio ranges, and the activities for panels A and B. Figure S2 contains two more experiments with a measured pH range falling between these two experiments. Water mole fractions ( $x_w$ ) were determined by converting molality of NaHSO<sub>4</sub> to mole fraction ( $x_{NaHSO4}$ ), then  $x_w = 1 - x_{NaHSO4}$ .

point optical trapping stability is impeded. The sodium bisulfate concentrations demonstrated here are 0.5 to 5.0 M (Figure S5). While these concentrations reach high acidity, the pH range is especially relevant to atmospheric aerosols. The measurable pH range accessible here is -0.36 to 0.76 using aqueous NaHSO<sub>4</sub>. Thus, a pH range of more than one complete unit can be directly measured using a single acidic probe molecule. This range can readily be expanded by using other acids with less acidic pK<sub>a</sub> values. If the individual Raman modes of the acid and conjugate base can be resolved, using multiple pH probe molecules in a single droplet to provide pH

measurements over an even wider range is also feasible.<sup>36</sup> Refractive indices of the individual components can be resolved using mixing rules developed for aerosol particles.<sup>57</sup>

# pH Measurements Accounting for Non-Ideal Thermodynamics.

The overall performance of directly measuring pH in the AOT is evaluated in Figure 4. The two representative experiments in Figure 3 and two more from Figure S2 are compared to thermodynamic predictions from the E-AIM model. On the left y-axis, the concentration ratios ([SO<sub>4</sub><sup>2-</sup>]/[HSO<sub>4</sub><sup>-</sup>]) from the optical tweezers time series shown in Figure 3 and Figure S2 are plotted versus the retrieved pH. The AOT data are plotted along with the E-AIM model output. The E-AIM curve shows the single solute NaHSO<sub>4</sub> (solid lines). On the right y-axis, the activity ratios are used instead of the concentration ratios after converting the anion molalities to activities in E-AIM. The pH and concentration ratios were collected for 100 frames at 0.5 Hz, totaling 200 seconds and binned by 0.03 pH units, and standard deviations due to statistical error in each bin are shown as error bars. Concentration ratio, [SO<sub>4</sub><sup>2-</sup>]/[HSO<sub>4</sub><sup>-</sup>], and the total anion concentration, [SO<sub>4</sub><sup>2-</sup>] + [HSO<sub>4</sub><sup>-</sup>], are independently measured; the former by applying a calibration curve based on bulk measurements, and the latter from the refractive indices through WGM analysis and the relationship between refractive indices and solute concentration. These two quantities are used to identify the concentrations for each anion to input into E-AIM and retrieve proton activities, a<sub>H+</sub>.

The scatter of concentration ratios for all pH measurements reported here result in an average error of  $\pm 0.32$  across the pH range of -0.36 to 0.76. The calculated activity ratios versus pH in these experiments fall close to the E-AIM curve with an average error of  $\pm 0.003$ . This value is much lower than our reported propagated error of  $\pm 0.03$  based on comparison with bulk

measurements. The error propagation and results for the pH measurements are described in the SI and discussed below.

The Henderson-Hasselbach equation, which does not consider the non-ideal effects of high molar total solute concentrations, predicts significantly higher concentration ratios and pH values than E-AIM because the pK<sub>a</sub> of HSO<sub>4</sub><sup>-</sup> is 2.0, so it is not displayed at these low pH values. In ideal

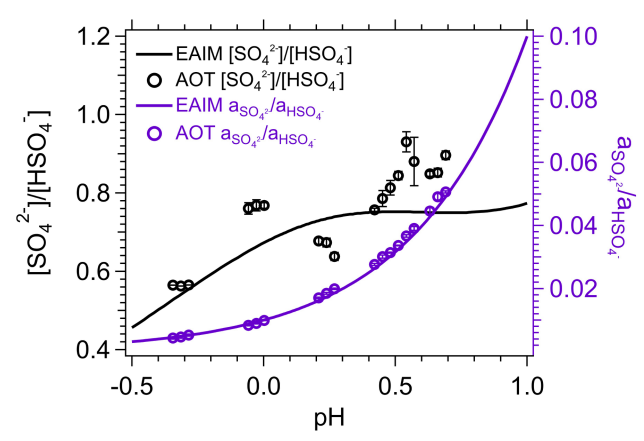


**Figure 4:** Concentration ratios (left y-axis) and activity ratios (right y-axis) versus pH in thermodynamic models (lines) and aerosol optical tweezers data (circles). Activity coefficients account for non-ideal interactions caused by high ionic strengths reached in the droplets, which result in consistent and accurate direct measurements of microdroplet pH.

solutions, the pH matches the pK<sub>a</sub> in the titration curve, yet we observe a lower pH transition region in the AOT experiments. This is due to non-ideal effects at these high solute concentrations, accounted for by thermodynamic model calculations. For example, the supplemental material of Guo et al. (Figure S1) discusses that the discrepancy between ideal and non-ideal bisulfate solutions is such that the non-ideal pK<sub>a</sub> occurs near pH  $\sim$  0. When pH is equal to the non-ideal pK<sub>a</sub>, the HSO<sub>4</sub><sup>-</sup> molecule accounts for 50% of the total sulfate as expected, whereas HSO<sub>4</sub><sup>-</sup> is almost 100% of the total sulfate population in an ideal solution. Clearly, the suppression of the dissociation of the HSO<sub>4</sub><sup>-</sup> anion apparent in high ionic strength droplets is due to the heightened activity of the H<sup>+</sup> ion, i.e. the low pH. Therefore, if non-ideal interactions are neglected in these highly acidic solutions, the sulfate/bisulfate ratios would be inaccurate and result in pH

measurements nearly 2 whole pH units higher. As shown in Figure 4, if the concentration ratios are converted to activity ratios by accounting for the total solute concentration, agreement is significantly improved between the E-AIM thermodynamic model and the experimental AOT data.

# **Discussion**

Figure 4 shows excellent agreement between the SO<sub>4</sub><sup>2</sup>-:HSO<sub>4</sub>- activity ratio, E-AIM, and the Henderson-Hasselbalch equation. The curves collapse almost perfectly onto a single curve when using activities because these systems are highly non-ideal, especially in the high solute concentration ranges studied here (1.0 M to 4.2 M droplets produced from 3.0 M to 8.0 M solutions). According to E-AIM thermodynamics, a lower pH transition occurs in this concentration range, much lower than the literature pK<sub>a</sub> value of 2.0, likely due to non-ideal intermolecular interactions in these highly concentrated solutions. Since pH is a measure of proton activity, rather than simply of proton concentration, <sup>60</sup> pH accounts for solution non-ideality as well. The activity approach in the right panel is therefore more suitable for evaluating our pH measurements. The accuracy of our pH measurements depends on the accuracy of the measured refractive indices, the anion peak area ratio calibration with anion concentration ratio, and the thermodynamic model E-AIM. The measurement uncertainties using our WGM fitting algorithm that we reported in Gorkowski et al.<sup>45</sup> are  $\pm 0.06\%$  in refractive index and  $\pm 0.05\%$  in particle diameter. Among the sources of error, the concentration ratios derived from the spontaneous Raman peak areas have the highest error (±0.32 averaged over 100 frames and with respect to E-AIM predictions), as shown in the visible scatter in the anion concentration ratio in Figure 4. The scatter is due to both the narrowness of the anion peaks, interference from WGMs passing through the anion Raman modes, and the small volume of the trapped droplets. Bisulfate is generally less intense in AOT measurements, which impacts the ratio calculation slightly in favor of sulfate.

Picoliter droplet volumes result in weaker individual anion Raman signals compared to our bulk calibration measurements, reducing the signal-to-noise ratio and resulting in pronounced scatter. Notably, the bulk Raman peak area ratios have far less scatter than for the microdroplets, as shown in Figure S5. The average statistical error over 100 frames for bulk measurements is  $\pm 0.02$  in the anion concentration ratio.

The low Raman signal issue could be overcome simply by increasing acquisition time, however the 2 second frame acquisition time we used is needed to capture the shifting spectral position of the WGMs. Prolonged acquisition spreads the WGMs and subsequently lessens the accuracy of their analysis, as the location of WGMs is critical for determination of radius and refractive index. Prior droplet pH measurements using Raman microspectroscopy by Rindelaub et al. 37 also used the distinguishable modes of  $v(SO_4^{2-})$  and  $v(HSO_4^{-})$  to measure the peak areas and calibrate them separately to relate them to [SO<sub>4</sub><sup>2</sup>-] and [HSO<sub>4</sub>-] using standard solutions containing MgSO<sub>4</sub> and H<sub>2</sub>SO<sub>4</sub>. However, because their droplets were deposited on a surface, WGMs do not manifest and therefore they used a longer acquisition time, resulting in stronger signal but without an independent measurement of total anion concentration. Their particle sizes (10-30 µm diameters) were 1.5-8 times larger than ours and their acquisition time (5 seconds) was twice as long as our AOT approach. The overall uncertainty in their pH measurements of 10-30 µm droplets on a substrate using Raman microscopy was not explicitly stated, but their statistical error varied from about  $\pm 0.02$  to  $\pm 0.2$  over a pH range of 0.19 to 0.79. It should be noted that their follow-up work reported by Craig et al.<sup>59</sup> used 3-5 μm diameter particles, closer to the 6-10 μm diameter particles used in this study, and saw similar effects and pH measurement uncertainties as this work obtained using AOT.

Although the anion peak area ratios arguably produce the most error in the direct pH measurement method developed here, the remaining quantities are derived from well-established experimental and theoretical procedures. E-AIM<sup>49–51</sup> is a rigorously vetted and widely used aerosol thermodynamics model suggested to be the most effective treatment for pH calculations among approximate and inferential methods, including ion balances and ion molar ratio.<sup>33</sup> Our results suggest that even including the dynamic behavior of the peak area ratios induced by WGMs and size effects, our pH measurement method works extremely well when combined with WGM analysis and thermodynamic models, empowering contactless single-particle techniques for observing pH dependent properties of microdroplets. The AOT method's uncertainty varied among the experiments, i.e. over different droplets. The lowest was  $\pm 0.03$  and the highest  $\pm 0.06$  pH units using a sodium bisulfate probe in the pH range of -0.36 to 0.76 when 100 Raman frames are acquired at 0.5 Hz over 3.3 minutes and averaged. The variation does not stem from the nature of the droplet; it is primarily due to the overall uncertainty being dominated by the WGM signal interference with the acid:base peak area ratios. It is difficult to control the level of WGM interference, which results in different uncertainties reported for different experiments. Averaging over 100 frames reduces the enhanced noise from WGM interference. The full error propagation method and results are provided in the SI.

The advantages in performing pH measurements in an optical tweezers are stable control of the isolated droplet for many hours if desired and the ability to directly probe the chemical environment of the particle with Raman scattering. 4,40–45 Analysis of the WGMs also determines the droplet's morphology, distinguishing between homogeneous and biphasic core–shell or partially engulfed microstructures. 4,44,45,3 The pH of the particle can influence the morphology and the segregation of liquid phases. 1,2 In fact, if two adjacent liquid phases are water-rich, they can have different pH levels. 61 In general, single-particle techniques allow access to information that

is inaccessible for bulk or ensemble populations, such as microphysical state including supersaturated metastable states, phase separation, and different morphologies. Aerosol optical tweezers coupled with cavity-enhanced Raman spectroscopy further offer the ability to control temperature, humidity, and chemical conditions in the trapping environment, and determine how these conditions alter the droplet's physicochemical properties, equilibration with the gas phase, and its chemical reactivity.

### **Conclusions**

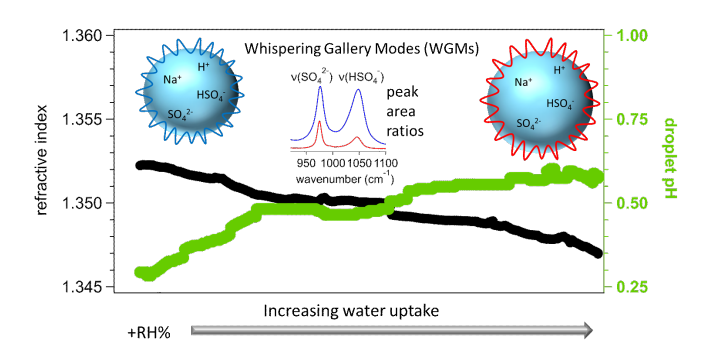
A new method for high accuracy direct measurements of the pH of levitated aqueous microdroplets was demonstrated using aerosol optical tweezers (AOT) and the cavity-enhanced Raman spectra retrieved. We achieve these measurements using two independently measured quantities uniquely obtained from the AOT: the refractive index of the solution droplets and the peak area ratio of the conjugate base versus acid Raman modes. The two quantities are used to obtain total solute concentration and concentration ratio, respectively. Concentrations of the acid molecule and its conjugate base are thus derived in real-time at 0.5 Hz. Refractive indices are measured through analysis of Whispering Gallery Modes (WGMs) within 0.06%, resulting in highly accurate determination of solute concentration to  $\pm 0.04$  M. We achieve uncertainties in pH measurements of picoliter droplets ranging from  $\pm 0.03$  to 0.06 pH units. This is similar to typically reported pH uncertainty levels of  $\pm 0.020$  for bulk measurements using spectroscopic techniques. Our pH measurements achieve low uncertainties, especially considering the differences in volume between these AOT (picoliters) and bulk (milliliters) experiments. This novel direct pH measurement method will provide new chemical insight into numerous pH-dependent processes known to occur in microdroplets and other confined chemical environments. This will advance our understanding of chemical phenomena such as the controls on phase separation and the nature of chemical reactions occurring in the bulk versus at interfaces, and the chemistry of atmospheric aerosol particles.

**Acknowledgments**. Hallie C. Boyer was supported by a Dreyfus Environmental Chemistry Postdoctoral Fellowship. This research was supported by the National Science Foundation (Awards CHE-1213718 and CHE-1554941). We appreciate valuable discussions regarding this methodology with Jonathan Reid. We acknowledge Darien Skifstad for collecting most of the data in Figure S2c.

**Competing Interests.** The authors declare no competing interests.

Supporting Information. The Supporting Information details the Raman measurements of bulk solutions to achieve calibration of sulfate:bisulfate concentration ratios of droplets in aerosol optical tweezers experiments. The Raman signals are shown (intensity vs. vibrational shift), as well as the linear relationship between peak area ratio measurements and concentration ratio. Comparison between peak area ratios of the bulk solutions and the microdroplets is shown. A Table of information includes experimental information such as solution concentration, number of frames, moving average window, and the composition and thermodynamic properties of the test droplets reported here. Error propagation methods are detailed and the results are provided for each experiment.

# TOC graphic



# References

- (1) Losey, D. J.; Ott, E. J. E.; Freedman, M. A. Effects of High Acidity on Phase Transitions of an Organic Aerosol. *J. Phys. Chem. A* **2018**, *122* (15), 3819–3828. https://doi.org/10.1021/acs.jpca.8b00399.
- (2) Losey, D. J.; Parker, R. G.; Freedman, M. A. pH Dependence of Liquid Liquid Phase Separation in Organic Aerosol. *J. Phys. Chem. Lett.* **2016**, *7* (19), 3861–3865. https://doi.org/10.1021/acs.jpclett.6b01621.
- (3) Gorkowski, K. J., Donahue, N. M. and Sullivan, R. C. Aerosol Optical Tweezers

  Constrain the Evolution of Liquid–Liquid Phase-Separated Morphologies in Atmospheric

  Particles. *Chem* **2019**, *in press*. https://doi.org/10.1016/j.chempr.2019.10.018.
- (4) Gorkowski, K.; Donahue, N. M.; Sullivan, R. C. Emulsified and Liquid–Liquid Phase-Separated States of α-Pinene Secondary Organic Aerosol Determined Using Aerosol Optical Tweezers. *Environ. Sci. Technol.* 2017, 51 (21), 12154–12163. https://doi.org/10.1021/acs.est.7b03250.
- (5) Banerjee, S.; Gnanamani, E.; Yan, X.; Zare, R. N. Can All Bulk-Phase Reactions Be Accelerated in Microdroplets? *Analyst* 2017, 142, 1399. https://doi.org/10.1039/c6an02225a.
- (6) Jacobs, M. I.; Davis, R. D.; Rapf, R. J.; Wilson, K. R. Studying Chemistry in Micro-Compartments by Separating Droplet Generation from Ionization. *Am. Soc. Mass Spectrom.* 2019, 30, 339–343. https://doi.org/10.1007/s13361-018-2091-y.
- (7) Wei, H.; Vejerano, E. P.; Leng, W.; Huang, Q.; Willner, M. R.; Marr, L. C.; Vikesland, P. J. Aerosol Microdroplets Exhibit a Stable PH Gradient. *Proc. Natl. Acad. Sci.* 2018, 201720488. https://doi.org/10.1073/pnas.1720488115.

- (8) Vaida, V. Prebiotic Phosphorylation Enabled by Microdroplets. *Proc. Natl. Acad. Sci.* 2017, 114 (47), 12359–12361. https://doi.org/10.1073/pnas.1717373114.
- (9) Li, Y.; Yan, X.; Cooks, R. G. The Role of the Interface in Thin Film and Droplet Accelerated Reactions Studied by Competitive Substituent Effects. *Angew. Chemie - Int.* Ed. 2016, 55 (10), 3433–3437. https://doi.org/10.1002/anie.201511352.
- (10) Lai, Y.-H.; Sathyamoorthi, S.; Bain, R. M.; Zare, R. N. Microdroplets Accelerate Ring Opening of Epoxides. *J. Am. Soc. Mass Spectrom* **1908**, *29*, 1036–1043. https://doi.org/10.1007/s13361-018-1908-z.
- (11) Gaston, C. J.; Riedel, T. P.; Zhang, Z.; Gold, A.; Surratt, J. D.; Thornton, J. A. Reactive Uptake of an Isoprene-Derived Epoxydiol to Submicron Aerosol Particles. *Environ. Sci. Technol.* **2014**, *48* (19), 11178–11186. https://doi.org/10.1021/es5034266.
- (12) Coddens, E. M.; Angle, K. J.; Grassian, V. H. Titration of Aerosol PH through Droplet Coalescence. *J. Phys. Chem. Lett.* **2019**, *10*, 4476–4483. https://doi.org/10.1021/acs.jpclett.9b00757.
- (13) Murray, B. J.; O'Sullivan, D.; Atkinson, J. D.; Webb, M. E. Ice Nucleation by Particles Immersed in Supercooled Cloud Droplets. *Chem. Soc. Rev* 2012, 41, 6519–6554. https://doi.org/10.1039/c2cs35200a.
- Boyer, H. C.; Dutcher, C. S. Atmospheric Aqueous Aerosol Surface Tensions: Isotherm-Based Modeling and Biphasic Microfluidic Measurements. *J. Phys. Chem. A* 2017, *121* (25). https://doi.org/10.1021/acs.jpca.7b03189.
- (15) Bain, R. M.; Pulliam, C. J.; Cooks, R. G. Accelerated Hantzsch Electrospray Synthesis with Temporal Control of Reaction Intermediates. *Chem. Sci.* **2015**, *6*, 391–401. https://doi.org/10.1039/c4sc02436b.

- (16) Lee, J. K.; Samanta, D.; Gil Nam, H.; Zare, R. N. Spontaneous Formation of Gold Nanostructures in Aqueous Microdroplets. *Nat. Commun. C* **2018**, *9* (1562), 1–9. https://doi.org/10.1038/s41467-018-04023-z.
- (17) Yan, X.; Bain, R. M.; Cooks, R. G. Organic Reactions in Microdroplets: Reaction Acceleration Revealed by Mass Spectrometry. *Angew. Chemie - Int. Ed.* 2016, 55 (42), 12960–12972. https://doi.org/10.1002/anie.201602270.
- (18) Jung, Y.; Marcus, R. A. On the Theory of Organic Catalysis "on Water." J. Am. Chem. Soc. 2007, 129, 5492–5502. https://doi.org/10.1021/ja068120f.
- (19) Fallah-Araghi, A.; Meguellati, K.; Baret, J. C.; El Harrak, A.; Mangeat, T.; Karplus, M.; Ladame, S.; Marques, C. M.; Griffiths, A. D. Enhanced Chemical Synthesis at Soft Interfaces: A Universal Reaction-Adsorption Mechanism in Microcompartments. *Phys. Rev. Lett.* 2014, *112* (2), 1–5. https://doi.org/10.1103/PhysRevLett.112.028301.
- (20) Nam, I.; Lee, J. K.; Gil Nam, H.; Zare, R. N. Abiotic Production of Sugar Phosphates and Uridine Ribonucleoside in Aqueous Microdroplets. *Proc. Natl. Acad. Sci.* **2017**, *114* (47), 12396–12400. https://doi.org/10.1073/pnas.1714896114.
- (21) Arak Freedman, M.; Ott, E.-J. E.; Marak, K. E. Role of PH in Aerosol Processes and Measurement Challenges. J. Phys. Chem. A 2019, 21. https://doi.org/10.1021/acs.jpca.8b10676.
- (22) Jha, I.; Rani, A.; Venkatesu, P. Sustained Stability and Activity of Lysozyme in Choline Chloride against PH Induced Denaturation. *Sustain. Chem. Eng.* **2017**, *5*, 8344–8355. https://doi.org/10.1021/acssuschemeng.7b02126.
- (23) Malevanets, A.; Chong, P. A.; Hansen, D. F.; Rizk, P.; Sun, Y.; Lin, H.; Muhandiram, R.; Chakrabartty, A.; Kay, L. E.; Forman-Kay, J. D.; Wodak, S. J. Interplay of Buried

- Histidine Protonation and Protein Stability in Prion Misfolding. *Sci. Rep.* **2017**, *7* (882), 1:14. https://doi.org/10.1038/s41598-017-00954-7.
- (24) Crans, D. C.; Levinger, N. E. The Conundrum of PH in Water Nanodroplets: Sensing PH in Reverse Micelle Water Pools. *Acc. Chem. Res.* **2012**, *45* (10), 1637–1645. https://doi.org/10.1021/ar200269g.
- (25) Lin, P. C.; Wu, Z. H.; Chen, M. S.; Li, Y. L.; Chen, W. R.; Huang, T. P.; Lee, Y. Y.; Wang, C. C. Interfacial Solvation and Surface PH of Phenol and Dihydroxybenzene Aqueous Nanoaerosols Unveiled by Aerosol VUV Photoelectron Spectroscopy. *J. Phys. Chem. B* 2017, 121 (5), 1054–1067. https://doi.org/10.1021/acs.jpcb.6b10201.
- (26) Wellen, B. A.; Lach, E. A.; Allen, H. C. Surface PKa of Octanoic, Nonanoic, and Decanoic Fatty Acids at the Air-Water Interface: Applications to Atmospheric Aerosol Chemistry. *Phys. Chem. Chem. Phys.* 2017, 19 (39), 26551–26558. https://doi.org/10.1039/C7CP04527A.
- (27) Jickells, T. D.; An, Z. S.; Andersen, K. K.; Baker, A. R.; Bergametti, G.; Brooks, N.; Cao, J. J.; Boyd, P. W.; Duce, R. A.; Hunter, K. A.; Kawahata, H.; Kubilay, N.; laRoche, J.; Liss, P. S.; Mahowald, N.; Prospero, J. M.; Ridgwell, A. J.; Tegen, I.; Torres, R. Global Iron Connections Between Desert Dust, Ocean Biogeochemistry, and Climate. *Science* (80-.). 2005, 308 (5718), 67–71.
- (28) Hung, H.-M.; Hoffmann, M. R. Oxidation of Gas-Phase SO 2 on the Surfaces of Acidic Microdroplets: Implications for Sulfate and Sulfate Radical Anion Formation in the Atmospheric Liquid Phase. *Environ. Sci. Technol.* 2015, 49, 13768–13776. https://doi.org/10.1021/acs.est.5b01658.
- (29) Lin, Y. H.; Zhang, Z.; Docherty, K. S.; Zhang, H.; Budisulistiorini, S. H.; Rubitschun, C.

- L.; Shaw, S. L.; Knipping, E. M.; Edgerton, E. S.; Kleindienst, T. E.; Gold, A.; Surratt, J. D. Isoprene Epoxydiols as Precursors to Secondary Organic Aerosol Formation: Acid-Catalyzed Reactive Uptake Studies with Authentic Compounds. *Environ. Sci. Technol.* **2012**, *46* (1), 250–258. https://doi.org/10.1021/es202554c.
- (30) Cheng, C.; Wang, G.; Meng, J.; Wang, Q.; Cao, J.; Li, J.; Wang, J. Size-Resolved Airborne Particulate Oxalic and Related Secondary Organic Aerosol Species in the Urban Atmosphere of Chengdu, China. *Atmos. Res.* **2015**, *161–162*, 134–142. https://doi.org/10.1016/j.atmosres.2015.04.010.
- (31) Liu, M.; Song, Y.; Zhou, T.; Xu, Z.; Yan, C.; Zheng, M.; Wu, Z.; Hu, M.; Wu, Y.; Zhu, T. Fine Particle PH during Severe Haze Episodes in Northern China. *Geophys. Res. Lett.* 2017, 44 (10), 5213–5221. https://doi.org/10.1002/2017GL073210.
- (32) Rapf, R. J.; Dooley, M. R.; Kappes, K.; Perkins, R. J.; Vaida, V. PH Dependence of the Aqueous Photochemistry of α-Keto Acids. *J. Phys. Chem. A* **2017**, *121* (44), 8368–8379. https://doi.org/10.1021/acs.jpca.7b08192.
- (33) Hennigan, C. J.; Izumi, J.; Sullivan, A. P.; Weber, R. J.; Nenes, A. A Critical Evaluation of Proxy Methods Used to Estimate the Acidity of Atmospheric Particles. *Atmos. Chem. Phys.* **2015**, *15* (5), 2775–2790. https://doi.org/10.5194/acp-15-2775-2015.
- (34) Weber, R. J.; Guo, H.; Russell, A. G.; Nenes, A. High Aerosol Acidity despite Declining Atmospheric Sulfate Concentrations over the Past 15 Years. *Nat. Geosci.* **2016**, *9* (4), 282–285. https://doi.org/10.1038/ngeo2665.
- (35) Sayer, R. M.; Gatherer, R. D. B.; Reid, J. P. A Laser Induced Fluorescence Technique for Determining the PH of Water Droplets and Probing Uptake Dynamics. *Phys. Chem. Chem. Phys.* 2003, 5 (17), 3740. https://doi.org/10.1039/b307002f.

- (36) Craig, R. L.; Nandy, L.; Axson, J. L.; Dutcher, C. S.; Ault, A. P. Spectroscopic Determination of Aerosol PH from Acid-Base Equilibria in Inorganic, Organic, and Mixed Systems. *J. Phys. Chem. A* 2017, *121* (30), 5690–5699. https://doi.org/10.1021/acs.jpca.7b05261.
- (37) Rindelaub, J. D.; Craig, R. L.; Nandy, L.; Bondy, A. L.; Dutcher, C. S.; Shepson, P. B.; Ault, A. P. Direct Measurement of PH in Individual Particles via Raman Microspectroscopy and Variation in Acidity with Relative Humidity. *J. Phys. Chem. A* 2016, 120 (6), 911–917. https://doi.org/10.1021/acs.jpca.5b12699.
- (38) Kyoo Lee, J.; Kim, S.; Gil Nam, H.; Zare, R. N.; Korea, O. Microdroplet Fusion Mass Spectrometry for Fast Reaction Kinetics. *Proc. Natl. Acad. Sci.* **2015**, *112* (13), 3898–3903. https://doi.org/10.1073/pnas.1503689112.
- (39) Nam, I.; Nam, H. G.; Zare, R. N. Abiotic Synthesis of Purine and Pyrimidine Ribonucleosides in Aqueous Microdroplets. *Proc. Natl. Acad. Sci.* 2017, 115 (1), 36–40. https://doi.org/10.1073/pnas.1718559115.
- (40) Butler, J. R.; Mitchem, L.; Hanford, K. L.; Treuel, L.; Reid, J. P. In Situ Comparative Measurements of the Properties of Aerosol Droplets of Different Chemical Composition. Faraday Discuss. 2008, 137, 351–366. https://doi.org/10.1039/b706770b.
- (41) Power, R. M.; Reid, J. P. Probing the Micro-Rheological Properties of Aerosol Particles Using Optical Tweezers. *Rep. Prog. Phys.* 2014, 77 (7), 074601. https://doi.org/10.1088/0034-4885/77/7/074601.
- (42) Power, R. M.; Burnham, D. R.; Reid, J. P. Toward Optical-Tweezers-Based Force Microscopy for Airborne Microparticles. *App. Opt.* **2014**, *53* (36), 8522–8534. https://doi.org/10.1364/AO.53.008522.

- (43) Mitchem, L.; Reid, J. P. Optical Manipulation and Characterisation of Aerosol Particles Using a Single-Beam Gradient Force Optical Trap. *Chem. Soc. Rev.* 2008, 37 (4), 756. https://doi.org/10.1039/b609713h.
- (44) Gorkowski, K.; Donahue, N. M.; Sullivan, R. C. Determination of Biphasic Core–Shell Droplet Properties Using Aerosol Optical Tweezers. *Environ. Sci. Process. Impacts* 2018. https://doi.org/10.1039/C8EM00166A.
- (45) Gorkowski, K.; Beydoun, H.; Aboff, M.; Walker, J. S.; Reid, J. P.; Sullivan, R. C. Advanced Aerosol Optical Tweezers Chamber Design to Facilitate Phase-Separation and Equilibration Timescale Experiments on Complex Droplets. *Aerosol Sci. Technol.* 2016, 50 (12), 1–15. https://doi.org/10.1080/02786826.2016.1224317.
- (46) Preston, T. C.; Reid, J. P. Accurate and Efficient Determination of the Radius, Refractive Index, and Dispersion of Weakly Absorbing Spherical Particle Using Whispering Gallery Modes. J. Opt. Soc. Am. B-Optical Phys. 2013, 30 (8), 2113–2122. https://doi.org/10.1364/josab.30.002113.
- (47) Preston, T. C.; Reid, J. P. Determining the Size and Refractive Index of Microspheres Using the Mode Assignments from Mie Resonances. *J. Opt. Soc. Am. A* **2015**, *32* (11), 2210. https://doi.org/10.1364/JOSAA.32.002210.
- (48) Tang, I. N.; Tridico, A. C.; Fung, K. H. Thermodynamic and Optical Properties of Sea Salt Aerosols. *J. Geophys. Res. Atmos.* **1997**, *102* (D19), 23269–23275. https://doi.org/10.1029/97JD01806.
- (49) Carslaw, K. S.; Clegg, S. L.; Brimblecombe, P. A Thermodynamic Model of the System HCI-HNO3-H2SO4-H2O, Including Solubilities of HBr, from 328 to 200 K, HBr Solubilities in Aqueous H2SO4 from ~240 to 205 K, and HNO3 Partial Pressures and

- Freezing Points for HNO3-H2S04-H20 Mixtures from 273.15 To. *J. Phys. Chem* **1995**, 99, 11557–11574.
- (50) Clegg, S. L.; Brimblecombe, P.; Wexler, A. S. Thermodynamic Model of the System H <sup>+</sup>
  -NH <sub>4</sub> <sup>+</sup> -SO <sub>4</sub> <sup>2-</sup> -NO <sub>3</sub> <sup>-</sup> -H <sub>2</sub> O at Tropospheric Temperatures. *J. Phys. Chem. A* **1998**,

  102 (12), 2137–2154. https://doi.org/10.1021/jp973042r.
- (51) Clegg, S. L.; Seinfeld, J. H.; Edney, E. O. Thermodynamic Modelling of Aqueous Aerosols Containing Electrolytes and Dissolved Organic Compounds. II. An Extended Zdanovskii-Stokes-Robinson Approach. *Aerosol Sci.* 2003, 34, 667–690. https://doi.org/10.1016/S0021-8502(03)00019-3.
- (52) Ault, A. P.; Guasco, T. L.; Ryder, O. S.; Baltrusaitis, J.; Cuadra-Rodriguez, L. A.; Collins, D. B.; Ruppel, M. J.; Bertram, T. H.; Prather, K. A.; Grassian, V. H. Inside versus
  Outside: Ion Redistribution in Nitric Acid Reacted Sea Spray Aerosol Particles as
  Determined by Single Particle Analysis. *J. Am. Chem. Soc.* 2013, 135 (39), 14528–14531.
  https://doi.org/10.1021/ja407117x.
- (53) Choi, B.-K.; Lockwood, D. J. *Ionic Conductivity and the Phase Transitions in Na2SO4;* 1989; Vol. 40.
- (54) Wills, J. B.; Knox, K. J.; Reid, J. P. Optical Control and Characterisation of Aerosol.
   Chem. Phys. Lett. 2009, 481 (4–6), 153–165. https://doi.org/10.1016/j.cplett.2009.09.020.
- (55) Miles, R. E. H.; Knox, K. J.; Reid, J. P.; Laurain, M. C.; Mitchem, L. Measurements of Mass and Heat Transfer at a Liquid Water Surface during Condensation or Evaporation of a Subnanometer Thickness Layer of Water. *Phys. Rev. Lett.* 2010, 105 (11). https://doi.org/10.1103/PhysRevLett.105.116101.
- (56) Murphy, J. G.; Gregoire, P. K.; Tevlin, A. G.; Wentworth, G. R.; Ellis, R. A.; Markovic,

- M. Z.; VandenBoer, T. C. Observational Constraints on Particle Acidity Using Measurements and Modelling of Particles and Gases. *Faraday Discuss.* **2017**, *200*, 379–395. https://doi.org/10.1039/c7fd00086c.
- (57) Liu, Y.; Daum, P. H. Relationship of Refractive Index to Mass Density and Self-Consistency of Mixing Rules for Multicomponent Mixtures like Ambient Aerosols. *J. Aerosol Sci.* **2008**, *39* (11), 974–986. https://doi.org/10.1016/j.jaerosci.2008.06.006.
- (58) Guo, H.; Nenes, A.; Weber, R. J. The Underappreciated Role of Nonvolatile Cations in Aerosol Ammonium-Sulfate Molar Ratios. *Atmos. Chem. Phys* **2018**, *18*, 17307–17323. https://doi.org/10.5194/acp-18-17307-2018.
- (59) Craig, R. L.; Peterson, P. K.; Nandy, L.; Lei, Z.; Hossain, M. A.; Camarena, S.; Dodson, R. A.; Cook, R. D.; Dutcher, C. S.; Ault, A. P. Direct Determination of Aerosol PH: Size-Resolved Measurements of Submicrometer and Supermicrometer Aqueous Particles. *Anal. Chem.* 2018, 90, 11232–11239. https://doi.org/10.1021/acs.analchem.8b00586.
- (60) Colussi, A. J. Can the PH at the Air/Water Interface Be Different from the PH of Bulk Water? https://doi.org/10.1073/pnas.1811632115.
- (61) Dallemagne, M. A.; Huang, X. Y.; Eddingsaas, N. C. Variation in PH of Model Secondary Organic Aerosol during Liquid-Liquid Phase Separation. *J. Phys. Chem. A* **2016**, *120* (18), 2868–2876. https://doi.org/10.1021/acs.jpca.6b00275.